

Opportunistic Screening at Abdominal CT: Use of Automated Body Composition Biomarkers for Added Cardiometabolic Value

Perry J. Pickhardt, MD

Peter M. Graffy, MPH

Alberto A. Perez, BE

Meghan G. Lubner, MD

Daniel C. Elton, PhD

Ronald M. Summers, MD, PhD

Abbreviations: DXA = dual x-ray absorptiometry, FRAX = Fracture Risk Assessment Tool, FRS = Framingham Risk Score, ROI = region of interest

RadioGraphics 2021; 41:524–542

<https://doi.org/10.1148/rg.2021200056>

Content Code: **PH**

From the Department of Radiology, University of Wisconsin School of Medicine & Public Health, E3/311 Clinical Science Center, 600 Highland Ave, Madison, WI 53792-3252 (P.J.P., P.M.G., A.A.P., M.G.L.); and Imaging Biomarkers and Computer-Aided Diagnosis Laboratory, Department of Radiology and Imaging Sciences, National Institutes of Health Clinical Center, Bethesda, Md (D.C.E., R.M.S.). Presented as an education exhibit at the 2019 RSNA Annual Meeting. Received March 29, 2020; revision requested August 15 and received August 28; accepted August 28. For this journal-based SA-CME activity, the authors P.J.P., M.G.L., and R.M.S. have provided disclosures (see end of article); all other authors, the editor, and the reviewers have disclosed no relevant relationships.

Address correspondence to P.J.P. (e-mail: ppickhardt2@uwhealth.org).

R.M.S. supported in part by the Intramural Research Program of the National Institutes of Health Clinical Center.

©RSNA, 2021

SA-CME LEARNING OBJECTIVES

After completing this journal-based SA-CME activity, participants will be able to:

- Discuss the potential benefits of CT-based opportunistic screening and the concerns related to incidental findings at imaging.
- Identify automated CT biomarkers that can be derived from abdominal CT examinations that are performed for other clinical indications.
- Describe how quantification of body composition measures at abdominal CT can be used for cardiometabolic risk stratification in patients.

See rsna.org/learning-center-rg.

Abdominal CT is a frequently performed imaging examination for a wide variety of clinical indications. In addition to the immediate reason for scanning, each CT examination contains robust additional data on body composition that generally go unused in routine clinical practice. There is now growing interest in harnessing this additional information. Prime examples of cardiometabolic information include measurement of bone mineral density for osteoporosis screening, quantification of aortic calcium for assessment of cardiovascular risk, quantification of visceral fat for evaluation of metabolic syndrome, assessment of muscle bulk and density for diagnosis of sarcopenia, and quantification of liver fat for assessment of hepatic steatosis. All of these relevant biometric measures can now be fully automated through the use of artificial intelligence algorithms, which provide rapid and objective assessment and allow large-scale population-based screening. Initial investigations into these measures of body composition have demonstrated promising performance for prediction of future adverse events that matches or exceeds the best available clinical prediction models, particularly when these CT-based measures are used in combination. In this review, the concept of CT-based opportunistic screening is discussed, and an overview of the various automated biomarkers that can be derived from essentially all abdominal CT examinations is provided, drawing heavily on the authors' experience. As radiology transitions from a volume-based to a value-based practice, opportunistic screening represents a promising example of adding value to services that are already provided. If the potentially high added value of these objective CT-based automated measures is ultimately confirmed in subsequent investigations, this opportunistic screening approach could be considered for intentional CT-based screening.

©RSNA, 2021 • radiographics.rsna.org

Introduction

Abdominal CT examinations contain robust information on body composition that is incidental to the clinical indication for imaging and generally goes unused in routine practice. There is growing interest in CT-based opportunistic screening, whereby these additional imaging data can be harnessed for assessment of patient risk and prediction of future adverse clinical events. These relevant biometric measures can now be fully automated through the use of artificial intelligence algorithms that provide rapid and objective assessment. Given that abdominal CT is used for a wide variety of clinical indications, a great opportunity exists for cardiometabolic screening that is incidental to the clinical question. In this review, we consider the clinical effect of abdominal CT in current medical practice and then delve into the issue of incidental findings, which has been viewed

TEACHING POINTS

- A strong case can be made for harnessing the rich incidental CT body composition data embedded in all abdominal examinations for clinical benefit.
- Examples of potential cardiometabolic screening opportunities at abdominal CT include assessment of bone mineral density for osteoporosis screening, quantification of aortic calcium for evaluation of cardiovascular risk, quantification of visceral and subcutaneous fat for evaluation of metabolic syndrome, assessment of muscle bulk and density for diagnosis of sarcopenia, and quantification of liver fat for diagnosis of hepatic steatosis.
- Fully automated CT-based bone measures compare favorably with the clinical reference standard fracture risk assessment tool (FRAX, University of Sheffield) for prediction of future osteoporotic fractures.
- The fully automated CT-based aortic calcification scoring algorithm demonstrated better performance than the multivariate FRS for both cardiovascular events and overall survival.
- CT-based measurement of visceral and hepatic fat will ultimately provide a more direct and useful definition of metabolic syndrome.

largely as a negative aspect. However, we examine the use of incidental CT data for beneficial opportunistic screening, with particular attention to fully automated measurement based on artificial intelligence. Rather than delve into the technical details of these automated algorithms, this review is instead focused more on the potential for clinical implementation of these CT-based measures of body composition.

Future directions for additional validation research and clinical implementation are explored. Ultimately, these tools could be used for large-scale population-based screening and individualized assessment of patient risk. Although the current concept focuses on an opportunistic approach, whereby the additional information is freely gathered with data that apply to the clinical indication, the possibility for intentional CT-based cardiometabolic screening in the future exists if the clear net clinical benefit and cost-effectiveness can be demonstrated.

Clinical Effect of Abdominal CT

Abdominal CT examinations are frequently ordered and performed throughout most of the industrialized world because they provide invaluable clinical information. In the United States alone (1), nearly 100 million body CT examinations are performed each year for a wide variety of clinical indications ranging from unexplained symptoms or a suspected abnormality to follow-up or surveillance of known conditions, including assessment of response to treatment. Despite concerns related to resource use, cost, and radiation exposure, the volume of CT examinations in

adult patients continues to climb (2). The ability of abdominal CT to allow detection or exclusion of relevant abnormalities renders it a high-value test. Along with the other cross-sectional imaging modalities, CT ranks as one of the major medical advances of the past one-half century. To date, most of the clinical benefit of CT has been appropriately focused on answering the specific clinical question. However, because of its comprehensive cross-sectional nature, abdominopelvic CT studies document all structures in the prescribed range of imaging, which can lead to incidental assessment of other regions.

Incidental Findings at Abdominal CT

The strength of CT, which is its ability to allow a broad survey of all abdominal and pelvic contents, has also been cited as a weakness. Unsuspected CT findings that are outside the purview of the clinical indication, which are often referred to as *incidentalomas*, have raised appropriate concern from referring providers for unleashing a cascade of unintended additional workups. Several radiologist-led efforts (3,4) have responded to these concerns with guidelines for rational management of incidental findings. For example, the often misunderstood *extracolonic findings* at CT colonography have been singled out by the Centers for Medicare & Medicaid Services as a major reason that this screening study remains uncovered for Medicare beneficiaries. In reality, unsuspected CT findings that are incidental to the reason for imaging have always been an issue that radiologists have managed. Through responsible handling that avoids defensive “overcalling,” with an understanding of the limitations of the technique and reservation of additional workup for incidentalomas with a legitimate chance for clinical relevance, the potentially negative aspects of incidental findings at CT can be effectively contained.

Opportunistic Screening at Abdominal CT

In comparison with the negative connotations of incidentalomas, a strong case can be made for harnessing the rich incidental CT body composition data embedded in all abdominal examinations for clinical benefit. We refer to this approach as *opportunistic screening*, whereby additional CT data that otherwise would typically go unused are leveraged. This CT-based opportunistic approach was initially focused on specific indications, such as extracolonic findings at CT colonography (5–7), but now more broadly applies to nearly any abdominal or chest CT examination.

A host of robust and objective CT-based biomarkers that were initially obtained with manual and semiautomated approaches such as

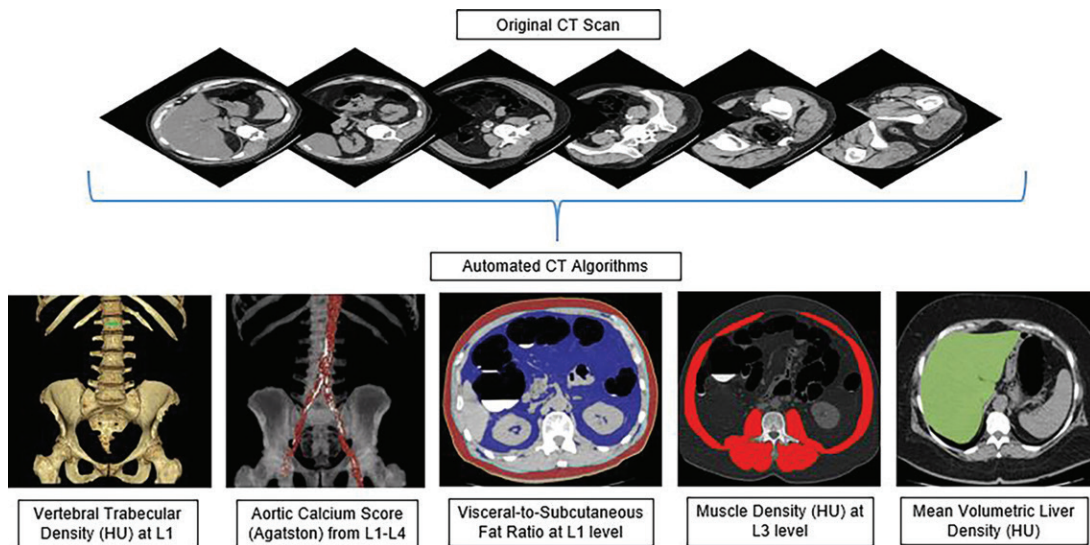


Figure 1. Automated CT-based cardiometabolic tools for assessment of (second row of images, left to right) bone, aortic calcium, visceral to subcutaneous fat ratio, muscle attenuation, and liver attenuation biomarkers from original abdominal CT data. In practice, a visual correlate allows for quality assurance for the automated segmentation results in individual patients. The specific CT biomarkers shown have all been validated in prior works. (Adapted and reprinted under a CC BY license from reference 23.)

region-of-interest (ROI) placement for attenuation data (in Hounsfield units) (8–12) can now be acquired with fully automated artificial intelligence–based tools. Of course, the reporting of radiologic imaging findings that are unrelated or incidental to the clinical indication predates CT, but this imaging modality is ideally suited for population-based opportunistic screening. Our group has developed, trained, tested, and validated various CT-based deep-learning and feature-based image processing algorithms (13–16). Analogous automated body composition tools are also being developed by other groups (17). After establishing normative population values, including changes in measures over time (18–22), we assessed the ability of these fully automated algorithms to predict future adverse events (23,24). In addition to further validation in more expanded and diverse patient cohorts, the next phase will likely involve actual clinical implementation.

Examples of potential cardiometabolic screening opportunities at abdominal CT include assessment of bone mineral density for osteoporosis screening, quantification of aortic calcium for evaluation of cardiovascular risk, quantification of visceral and subcutaneous fat for evaluation of metabolic syndrome, assessment of muscle bulk and density for diagnosis of sarcopenia, and quantification of liver fat for diagnosis of hepatic steatosis (Fig 1). Each of these biometric measures is discussed in more detail. Note that the predictive performance of these automated CT-based tools can be further enhanced by combining their complementary value. Our initial experience has largely focused on noncontrast-

enhanced abdominal CT examinations performed in asymptomatic individuals in a screening cohort (ie, for colorectal cancer screening), but these tools and measures can be adapted for use in contrast-enhanced CT studies (25–27).

Assessment of Bone Mineral Density

Osteoporosis is a highly prevalent public health concern that is associated with a large economic burden (28,29). Complicating fragility fractures result in substantial morbidity and mortality, and up to 30% of patients die within 1 year of an osteoporotic hip fracture (30). Unfortunately, osteoporosis is also a grossly underdiagnosed and undertreated condition, with screening rates that continue to lag (31), and additional means of detection are needed. Osteoporosis has also been underrecognized in men, because approximately one-half of all men older than 50 years have low bone mineral density (ie, osteopenia or osteoporosis), which is similar to the data for women (32). All of this represents an ideal situation for CT-based opportunistic screening (33).

Body CT examinations contain rich bone mineral density data and are disproportionately performed in older adults. CT also offers advantages over dual x-ray absorptiometry (DXA), which is the current clinical reference standard but yields false-negative results in most patients with osteoporotic fractures (8,34). Given the volumetric nature of CT, direct assessment of the vertebral trabecular space avoids the overlying cortical bone that a planar study such as DXA cannot. CT-based assessment of bone mineral density can be either an intended examination,

referred to as *quantitative CT*, or serve as an additional study performed for other reasons (ie, opportunistic screening).

As with central DXA, assessment of bone mineral density at abdominopelvic CT can include either the lumbar spine or the hip. Although CT can provide DXA-equivalent T-scores of the femoral neck (35,36), this approach essentially treats CT as a planar examination, along with its inherent weaknesses. A quicker, more direct, and likely more sensitive approach to opportunistic bone mineral density screening simply involves placing an ROI in the anterior trabecular space of the L1 vertebral body (Fig 2a) (37). We and others (8,37–40) have gathered substantial experience with this L1 trabecular attenuation measurement, including age-related normative values, as shown in Figure 2b. Although any vertebral level from T12 through L5 could be used, we have focused on L1 because it is present on both thoracic and abdominal CT images, is easily recognized as the first nonrib-bearing vertebra, and is generally less angled to the axial (transverse) plane compared with L5. ROI placement can be made on either the axial or sagittal view (41), but the latter allows concurrent evaluation for prevalent compression fractures (42). As shown in Figure 2, an ovoid ROI measuring 100–200 mm² is placed in the anterior aspect of the L1 trabecular space, subjacent to the cortical bone. Unlike formal quantitative CT, on-the-fly placement of an ROI does not require angling the plane parallel with the disc space yet generates similar results (7). As a general rule, L1 trabecular attenuation less than 100 HU at 120 kVp is relatively specific (ie, approximately 90%) for osteoporosis according to DXA results, whereas attenuation less than 150 HU generally correlates with low bone mineral density (ie, osteopenia or osteoporosis), and is approximately 90% sensitive for osteoporosis based on assessment with DXA (8,39). However, because planar DXA is an imperfect reference standard, CT assessment likely allows better stratification of patients at risk for fracture (8). More importantly, 90 HU appears to be an optimal threshold for determining the risk of osteoporotic fracture (43).

Measurement of L1 trabecular attenuation at CT can be fully automated (Figs 3, 4) (16,21). We have used a feature-based image processing algorithm that begins with automated spine segmentation and labeling to identify each vertebral level from T12 to L5. This step is followed by isolation of the anterior trabecular space of each vertebra, with the use of the L1 vertebra whenever possible (Figs 3, 4). The automated L1 attenuation value has shown good agreement with data from manual ROI placement (21). For older adults, in whom assessment of

bone mineral density is most valuable, the effect of intravenous contrast material enhancement appears to be less than that for younger patients, for the purposes of opportunistic screening (37,44). Nonetheless, a linear correction factor for the effect of intravenous contrast material on attenuation values may be incorporated (25). As with manual assessment of the ROI, automated measurement of L1 attenuation values is valuable for identification of patients at risk for future major osteoporotic fractures. In fact, both our group (24) and another group (45) have recently demonstrated that fully automated CT-based bone measures compare favorably with the clinical reference standard Fracture Risk Assessment Tool (FRAX, University of Sheffield) for prediction of future osteoporotic fractures (Figs 3, 4). In addition, when automated assessment of muscle is included, the diagnostic performance of CT further improves. This performance of automated CT is remarkable, because the clinical FRAX tool is a somewhat onerous online calculator that requires gathering and manually inputting multiple clinical variables for each patient.

The sagittal view of the spine allows accurate identification of vertebral compression fractures, most of which are missed on the axial view at standard interpretation (42). As is the case with trabecular attenuation, detection of fractures can also be fully automated with artificial intelligence methods (Fig 5) (45,46). In addition to the importance of detection of symptomatic fractures and confirmation of complicated osteoporosis, the greatest risk factor for a future osteoporotic fracture is a prior fracture.

Aortic Calcium Scoring

Cardiovascular disease remains the leading cause of death, both in the United States and globally. Cardiovascular disease affects more than 90 million Americans, and nearly one-half of all adults are expected to have some form of heart disease by 2030 (47,48). In 2015 alone, heart disease and stroke accounted for more than 630 000 and 140 000 deaths in the United States, respectively (49). Accurate assessment of risk for future cardiovascular events helps to guide appropriate patient treatment, including more aggressive treatments for those at highest risk and protection from the costs and complications related to unnecessary interventions for those at lower risk. In particular, presymptomatic detection of increased risk could lead to important preventive measures, such as initiation of statin therapy.

Conventional approaches to cardiovascular risk assessment such as the Framingham risk score (FRS) consist of multivariate measures based on

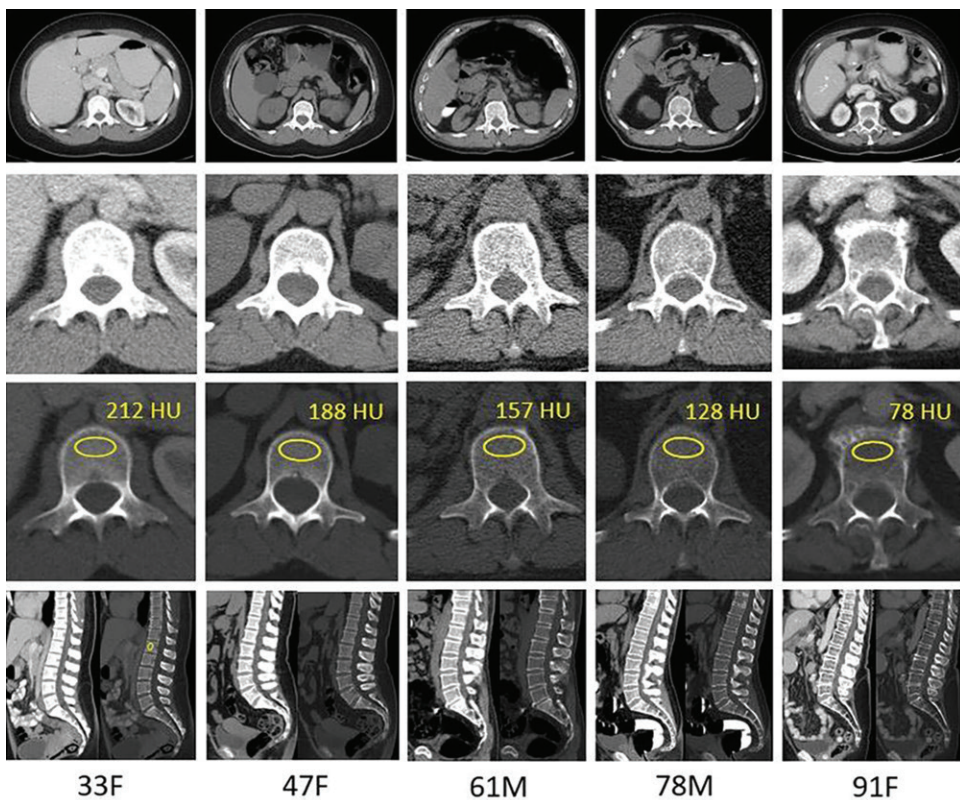
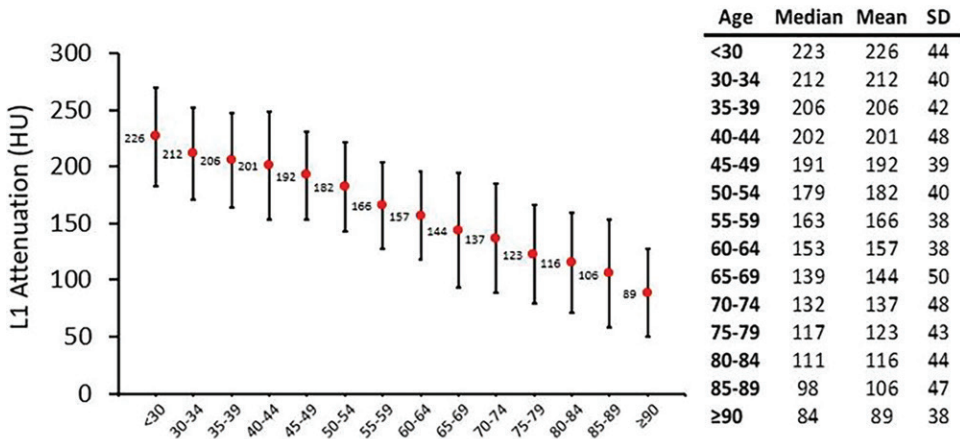
**a.****b.**

Figure 2. (a) CT-based assessment of bone mineral density with the use of trabecular attenuation at the L1 vertebral level. Axial CT images show the L1 vertebral level (top row) in adult patients of a variety of ages. Magnified axial CT views show the L1 vertebra in soft tissue (second row) and bone (third row) windows. Standard manual placement of the ROI for measurement of trabecular attenuation and the mean attenuation value in the ROI are shown in the third row. Automated ROI placement was programmed to match this location. Sagittal reconstruction images (bottom row, soft-tissue [left] and bone [right] windows) show placement of the ROI (yellow oval) at the L1 vertebra. Typically, trabecular attenuation values progressively decrease with increasing patient age. The loss of bone mineral density is more apparent with the soft-tissue window. (Reprinted, with permission, from reference 39.) (b) Graph (left) shows normative reference CT-based L1 trabecular attenuation values based on more than 20 000 examinations. The mean attenuation values show that age-related L1 trabecular bone loss is fairly linear. Error bars indicate standard deviations, which are remarkably uniform throughout the age spectrum. Table (right) shows the median and the mean (\pm standard deviation [SD]) values for L1 trabecular attenuation for each age group. These normative reference ranges, which are derived from a combination of manual and automated measurements, can serve as a quick reference for radiologists when reading body CT examinations performed for other clinical indications. Note that these values apply to scanning at 120 kVp. (Reprinted, with permission, from reference 37.)

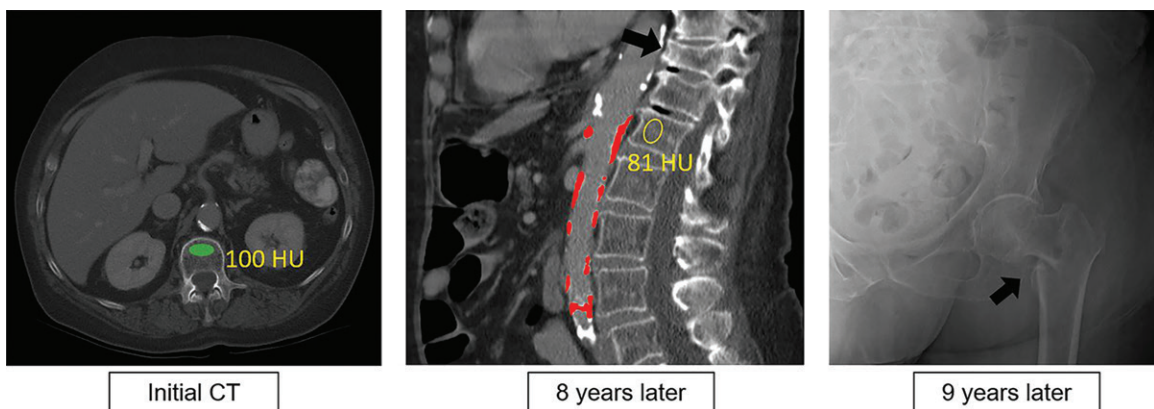


Figure 3. Opportunistic CT measurement of L1 trabecular attenuation in an asymptomatic 76-year-old woman who presented with abdominal pain due to mild pancreatitis. Axial contrast-enhanced CT image (left) shows the relative placement of the automated bone mineral density ROI (green oval) in the anterior trabecular space of the L1 vertebral body. An attenuation value of 100 HU indicates low bone mineral density. Placement of the ROI was intended to match that placed with the previously established manual approach. Sagittal CT image (middle) from an examination performed 8 years later for unintended weight loss shows manual placement of the L1 ROI and an attenuation value of 81 HU, which indicates osteoporosis. An interval vertebral compression fracture at T11 (arrow) is now seen. Note also the depiction of abdominal aortic calcium quantification (red shading) between the L1 and L4 vertebral levels. Frontal radiograph (right) obtained 9 years after the initial CT examination shows a left hip fracture (arrow), the risk for which could have been identified at an earlier CT examination.

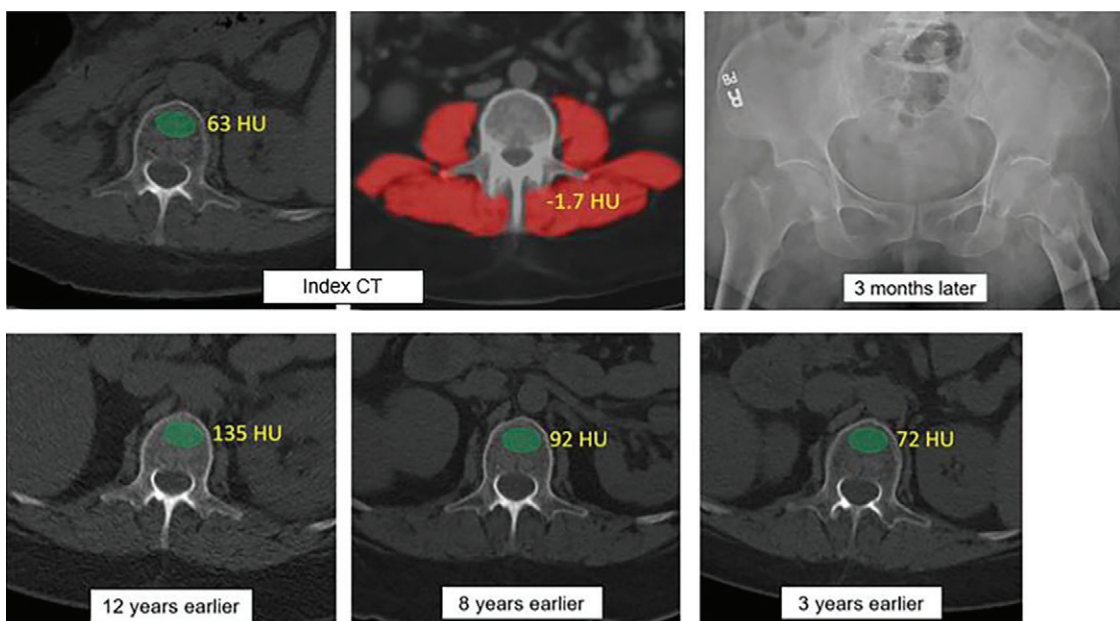


Figure 4. CT for prediction of an osteoporotic fracture in an asymptomatic 59-year-old woman undergoing colorectal cancer screening. Index axial CT images (top row, left and middle) show results from automated assessment of bone with the automated placement of the bone mineral density ROI (green oval, top row, left) (63 HU) and muscle (-1.7 HU) attenuation (red shading, top row, middle), which were in the 99th and 98th percentiles, respectively, relative to the entire screening study cohort. However, the 10-year FRAX scores for this patient were 6.7% for any fracture and 0.5% for hip fracture, which are results well below the recommended treatment threshold. Frontal radiograph (top row, right) from 3 months later shows that the patient sustained a left femoral neck fracture. Axial noncontrast CT images (bottom row) from multiple prior examinations for urolithiasis over the years show, in retrospect, a progressive decrease in L1 bone attenuation at the ROI (green oval, automated measures shown). Unfortunately, this information is typically not considered in routine clinical practice for CT examinations performed for other indications. (Adapted and reprinted, with permission, from reference 24.)

traditional clinical risk factors such as age, sex, cholesterol level, and blood pressure results (50). However, use of these clinical prediction models tends to place large numbers of patients into an intermediate risk category, prompting the need for additional noninvasive measures (51). Among

these additional measures is CT-based quantification of coronary artery calcification, which is an independent predictor of cardiovascular risk (52,53). Atherosclerotic calcification of the abdominal aorta also correlates with coronary artery disease (54). We found that a single measure of a

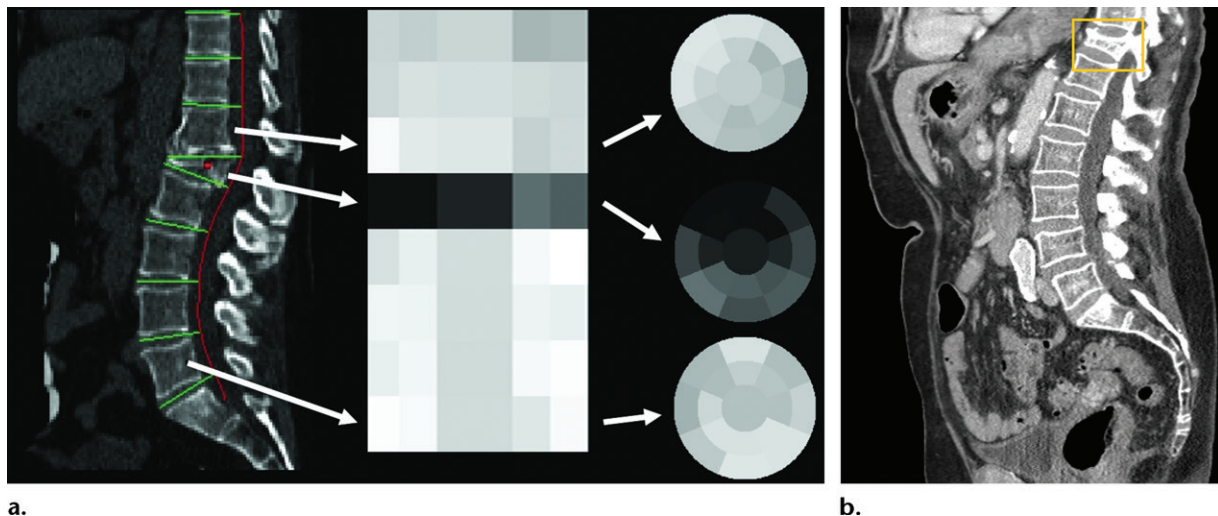


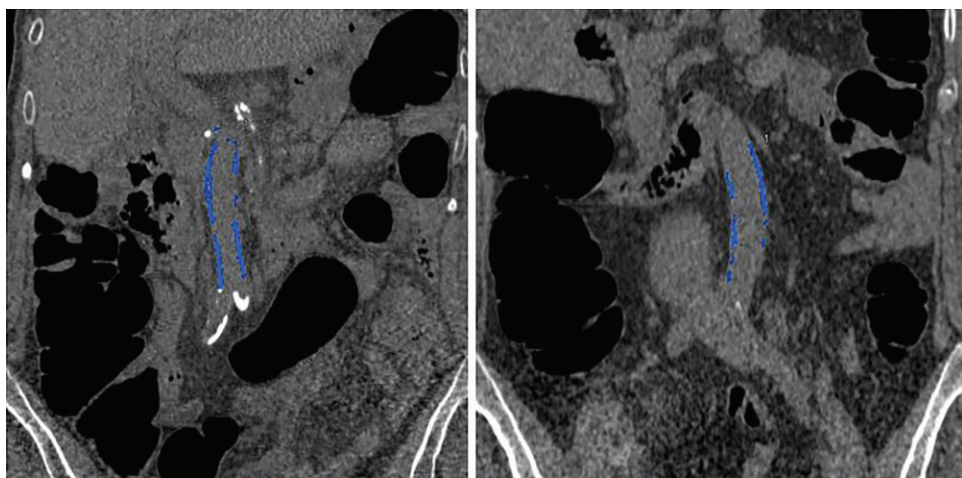
Figure 5. Automated detection of a vertebral fracture with two different algorithms in two patients. (a) Composite CT image in a 62-year-old woman with a severe osteoporotic compression fracture of the L1 vertebral body shows the use of an algorithm for automated detection and characterization of fractures that involves the use of a height compass approach (red and green lines, left). The geometric arrangement of the compass-like layout consists of a central circular sector surrounded by two ring-shaped finite thickness concentric bands. The sagittal CT image (left) shows vertebral column segmentation and partitioning. The adjacent image (right) shows the stacked-height compass of the entire vertebral column. The circular images show the height compasses for a grade-3 wedge fracture at L1 (middle) and preserved vertebral height at T12 (top) and L5 (bottom). The patient underwent spine DEXA less than 2 months earlier that was interpreted as normal (T-score, -0.5). (b) Sagittal CT image in an 85-year-old woman shows a severe T11 compression deformity (yellow rectangle), which was detected with a different automated deep-learning algorithm. (Fig 5b courtesy of Einav Blumenfeld, Zebra Medical Systems.)

noncontrast CT-based abdominal aortic calcification score that was acquired with a semiautomated method outperformed the FRS for prediction of future cardiovascular events in a screening cohort, with an average of more than a decade of follow-up (Fig 6), (12). At a threshold Agatston score of 200, CT-based quantification of abdominal aortic calcification showed a net improvement of 35% in the accuracy of classification over that of FRS alone for 5-year risk, and it was evenly balanced between event and nonevent improvement with reclassification. In comparison, adding FRS to the CT-based aortic calcification score did not provide additional benefits (Fig 6) (12).

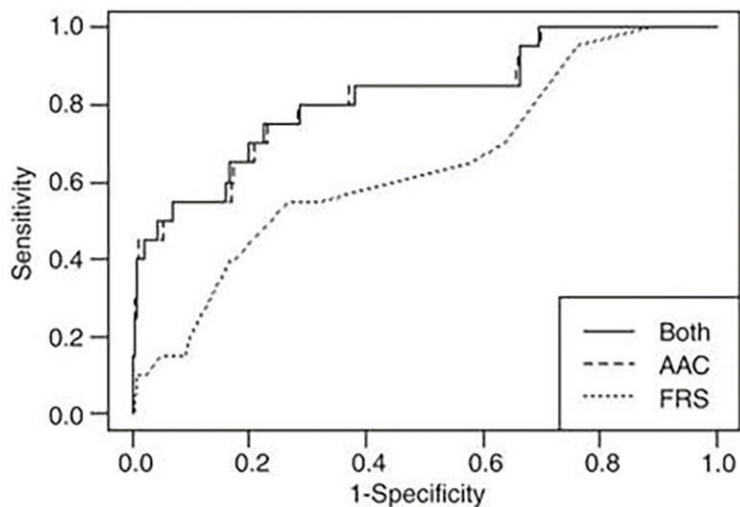
To automatically segment and quantify calcified atherosclerotic plaque involving the abdominal aorta at CT, we applied a deep-learning mask R-CNN (region-based convolutional neural networks) algorithm (18). Unlike the semiautomated method, in which the user selects the coverage to include the entire abdominal aorta to the bifurcation, the automated algorithm is designed to segment and quantify aortic calcium at the L1-L4 vertebral levels (Fig 7). Nonetheless, good agreement was observed between these semiautomated and automated methods. As with the other artificial intelligence-based algorithms, this automated version allows for large-scale population-based assessment (Fig 8). Previously, automated evaluation of aortic calcification was only demonstrated for noncontrast CT, but a newer method involving the use of a three-dimensional U-Net has now

been validated for use with contrast-enhanced CT (26). Similar to the predictive ability shown with the semiautomated approach, the fully automated CT-based aortic calcification scoring algorithm demonstrated better performance than that of the multivariate FRS for both cardiovascular events and overall survival. For example, the highest-risk quartile based on automated classification of CT-based aortic calcification (Agatston score > 492) was associated with a hazard ratio for death of 4.5 relative to the other three quartiles, whereas the corresponding hazard ratio for FRS was 2.8 (Fig 9) (23). Furthermore, the 5-year area under the receiver operating characteristic (ROC) curve for overall survival was 0.74 for aortic calcification, compared with 0.69 for FRS. As seen with fracture prediction, combining different automated CT-based measures can further improve performance for prediction of cardiovascular events and death. For example, the 2-year area under the ROC curve for overall survival increases to 0.81 when CT-based aortic calcification, visceral fat, and liver fat are combined (Figs 10, 11) (23).

A case can also be made for opportunistic quantification of coronary artery calcium identified at abdominal CT. It has been shown that coronary calcium scoring with the use of low-dose noncontrast chest CT performed without electrocardiographic gating correlates well with the results of dedicated gated coronary calcium scoring protocols (55). Although the entire heart is typically not included in abdominal CT protocols,



a.



b.

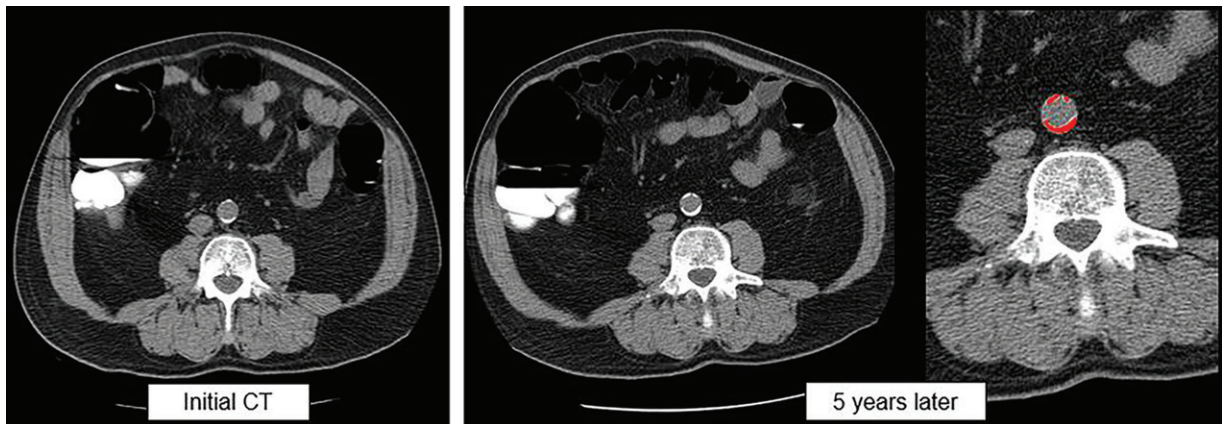


Figure 7. Change in the automated abdominal aortic calcium level over time in an asymptomatic 60-year-old man undergoing noncontrast CT for colonographic screening. Axial image from index CT examination (left) shows moderate hard plaque involving the abdominal aorta, which corresponds to an automated Agatston score of 1514. Axial CT images acquired 5 years later (middle and right) show an interval increase in hard plaque (red shading, right) that corresponds to an automated Agatston score of 5070. The patient experienced a myocardial infarction 4 years after the second CT examination and developed congestive heart failure 3 years after that.

if an Agatston score of the visualized coronary arteries exceeds a relevant threshold, such as greater than 100 and greater than 400 for intermediate and high risk, respectively, this could add diagnos-

tic value. Automated algorithms with the use of deep learning allow detection and quantification of the coronary calcium load at nongated CT (Fig 12) (56,57).

Figure 8. Bar graph shows automated population-based assessment of abdominal aortic calcium scoring at noncontrast CT and progressive increases in mean abdominal aortic calcium scores from a generally healthy screening population of nearly 10000 adults. Agatston scores in women lag by nearly a decade behind those for men. More than 30% of all individuals had an Agatston score of zero, more than 50% had a score less than 100, and nearly 70% had a score less than 300, whereas more than 30% had a score greater than 300. Of note, greater than 90% of this screening cohort was younger than 70 years of age, which explains the lower frequency of higher Agatston scores. (Reprinted, with permission, from reference 18.)

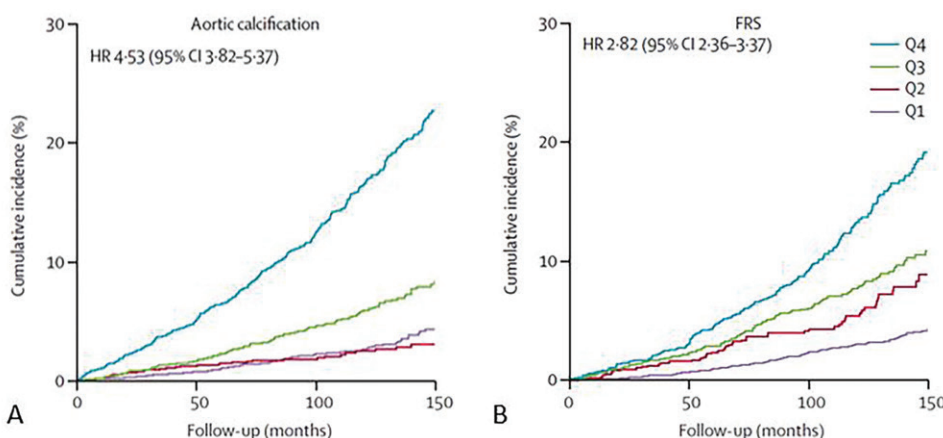
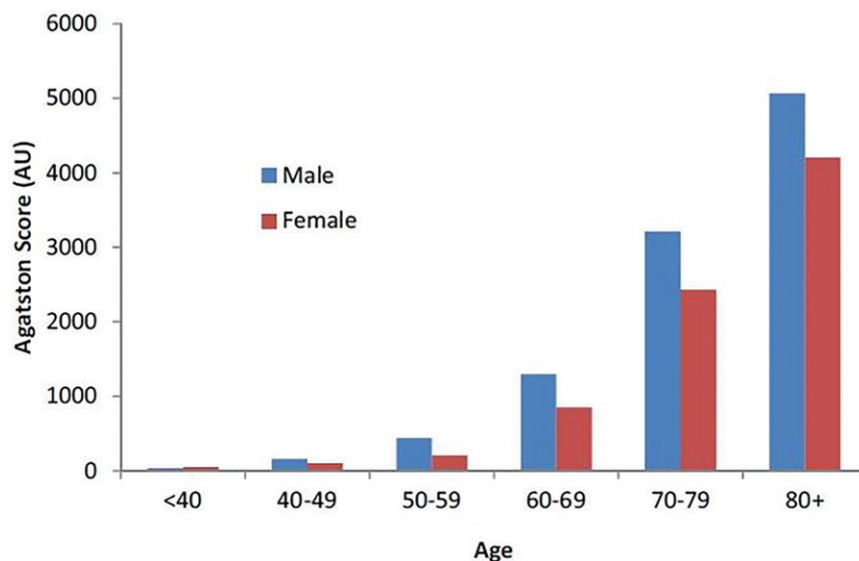


Figure 9. Kaplan-Meier time-to-death plots by quartile for, *A*, automated CT-based aortic calcium scores and, *B*, FRSs in a cohort of asymptomatic adults. Note that the separation for the highest-risk quartile (Q4, corresponding to an Agatston score > 492) is greater for automated aortic calcium scoring alone than that with the multivariate FRS. This difference is also reflected in the larger hazard ratio for aortic calcification than that for the FRS (4.5 vs 2.8). (Adapted and reprinted under a CC BY license from reference 23.)

Quantification of Visceral and Subcutaneous Fat

Intra-abdominal or visceral fat is now widely recognized to be highly relevant to both cardiovascular risk and metabolic syndrome (58–60). However, because visceral fat cannot be measured with standard clinical (ie, nonimaging) means, it is not a defining criterion for central obesity, which is poorly assessed with body mass index or waist circumference (59). In addition, ectopic fat, particularly hepatic steatosis, is also not a defining element for metabolic syndrome but, similar to visceral fat, is also considered to be highly relevant. Of course, both visceral and hepatic fat can be readily derived from cross-sectional imaging such as CT and MRI and have been correlated with metabolic syndrome (Fig 13) (11).

A variety of semiautomated and fully automated tools exist for measurement of both sub-

cutaneous and visceral fat at abdominal CT (Fig 13) (11,17,22,61). Somewhat analogous to the apple- versus pear-shaped body habitus, use of the CT biomarker of the visceral to subcutaneous fat ratio allows a more quantitative assessment of these subjective descriptors (Fig 13) (22). As with the other automated CT-based tools, population-based studies can effectively show sex-related differences in the distribution of subcutaneous and visceral fat (Fig 14). In our healthy outpatient adult screening cohort, the mean visceral to subcutaneous fat ratio was 1.8 in men and 0.6 in women (22). This automated CT tool can also allow objective measurement of changes in abdominal fat over time. We have shown that accounting for the specific distribution of abdominal fat (ie, visceral vs subcutaneous) provides much more valuable information than body mass index alone for prediction of future cardiovascular events and

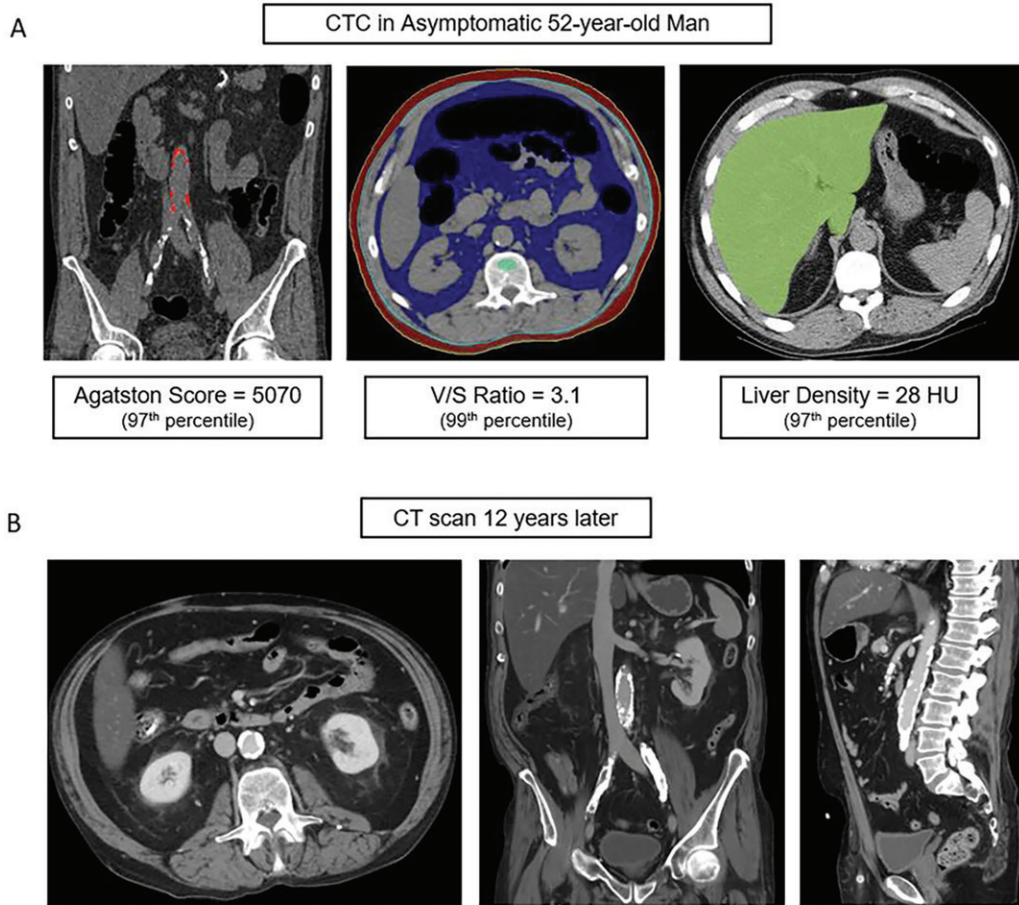


Figure 10. Combining automated CT tools for prediction of future adverse events in an asymptomatic 52-year-old man undergoing CT colonography (CTC) for colorectal cancer screening. *A*, Coronal (left) and axial (middle and right) screening images show calcification (red shading, left), the visceral (blue shading, middle) to subcutaneous (red shading, middle) fat ratio, and liver attenuation (green shading). This patient had a body mass index of 27.3 and an FRS of 5% (low risk). However, several CT-based metabolic markers were indicative of underlying disease (values and percentiles provided). The patient had an acute myocardial infarction 3 years after this initial CT examination and died 12 years after the initial CT examination at the age of 64 years. *B*, Axial (left), coronal (middle), and sagittal (right) contrast-enhanced CT images acquired for minor trauma 7 months before death were interpreted as negative for abnormalities but show substantial progression of vascular calcification, visceral fat, and hepatic steatosis. (Adapted and reprinted under a CC BY license from reference 23.)

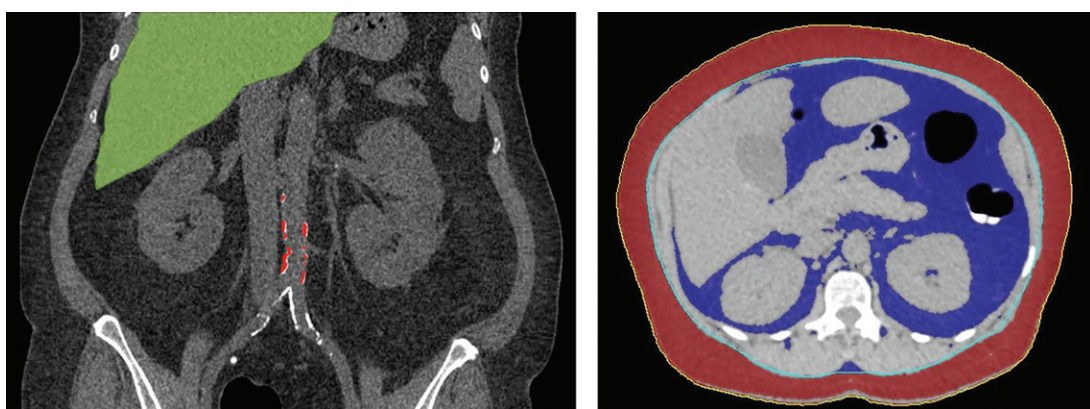


Figure 11. Automated body composition tools for metabolic syndrome in an asymptomatic 60-year-old woman. Coronal noncontrast (left) and axial (right) CT images show liver attenuation (green shading), aortic calcium (red shading, left), and abdominal segmentation and quantification of visceral (blue shading, right) and subcutaneous (red shading, right) fat. In this case, automated mean liver attenuation was 34 HU (95th percentile), which indicates moderate to severe steatosis. The automated Agatston score was 2781 (92nd percentile), and the automated L1-level visceral fat area was 326 cm² (95th percentile for women, 91st percentile overall). This patient had a myocardial infarction 3 years after the CT examination and died within 1 year after that.

Figure 12. Non-gated coronary calcium scoring. Noncontrast CT image obtained without gating in a 71-year-old man shows automated segmentation of left coronary artery calcification (orange shading) with a validated deep-learning algorithm. The Agatston score was 611. Although most abdominal CT examinations do not include imaging the heart in its entirety, even partial coverage showing a calcium score greater than 400 signifies a high risk for a future adverse event. (Case courtesy of Einav Blumenfeld, Zebra Medical Systems.)

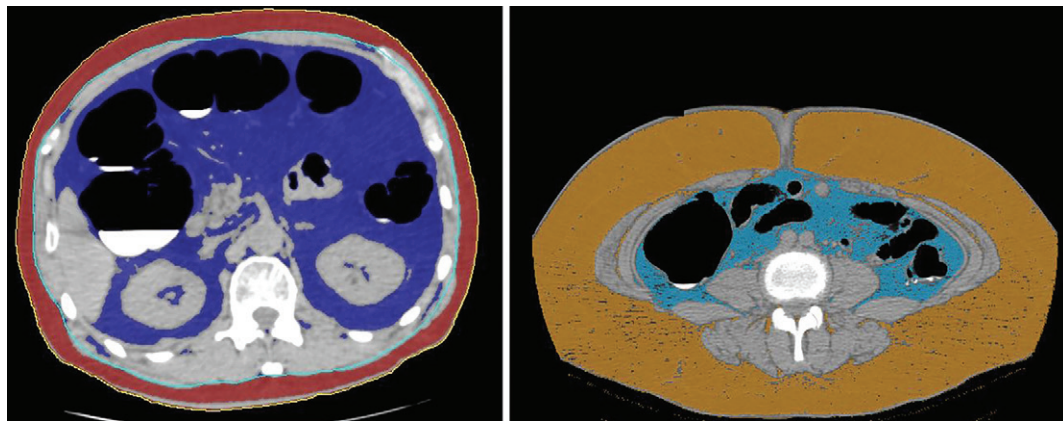
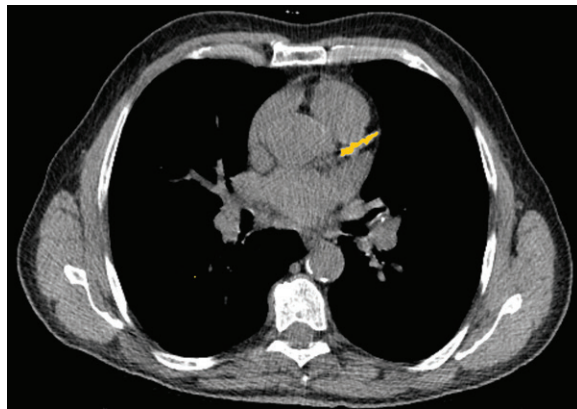


Figure 13. Visceral and subcutaneous fat segmentation and quantification at CT in two asymptomatic obese adults with similar body mass index levels but different body habitus. Axial CT image (left), which was acquired with the use of the automated fat tool in a 67-year-old man, shows a relative abundance of visceral fat (blue shading) compared with subcutaneous fat (red shading), whereas the other axial CT image (right), for which an earlier semiautomated fat tool was used at the umbilical level in a 52-year-old woman, shows a relative abundance of subcutaneous fat (orange shading) in comparison to visceral fat (light blue shading). These findings show the difference between so-called apple- and pear-shaped body habitus, respectively. This difference can be quantified with the visceral to subcutaneous fat ratio. The increased visceral to subcutaneous fat ratio for the patient on the left portends a higher cardiovascular risk.

death (Fig 15). For example, for prediction of overall survival, the 5-year area under the ROC curve for the automated CT-based visceral to subcutaneous fat ratio was 0.66, compared with only 0.50 for body mass index (23). CT-based fat measures can also be combined with other automated biomarkers to enhance predictive performance (Figs 10, 11). On the basis of our initial experience, we believe that CT-based measurement of visceral and hepatic fat will ultimately provide a more direct and useful definition of metabolic syndrome (60). In addition to quantification of the amount of visceral fat, some authors (62) have suggested that its attenuation may also be a relevant measure, although this could be due, in part, to its expected inverse relationship with the amount of fat.

Assessment of Muscle Bulk and Density

Sarcopenia refers to muscle wasting that occurs with normal aging, but it can also be accelerated

by a variety of disease processes. Innumerable studies have demonstrated the prognostic value of muscle assessment for prediction of outcomes before cancer therapy (63) and for other clinical scenarios such as postoperative complications and a host of chronic medical conditions (40). We have developed a deep-learning algorithm that consists of a modified three-dimensional U-Net for automatic segmentation and analysis of the abdominal wall musculature at CT (13,19). CT is a useful tool for assessment of the abdominal wall musculature, including both muscle bulk (measured indirectly as cross-sectional area or volume) and muscle density (soft tissue vs fat measured indirectly with attenuation values in Hounsfield units) (Fig 16) (19). Along with others (17), we have selected the L3 vertebral level for standardized evaluation of muscle at CT, because this level provides optimal inclusion of the psoas, paraspinal, and abdominal wall musculature.

We have found that CT-based muscle attenuation decreases more rapidly with age than does

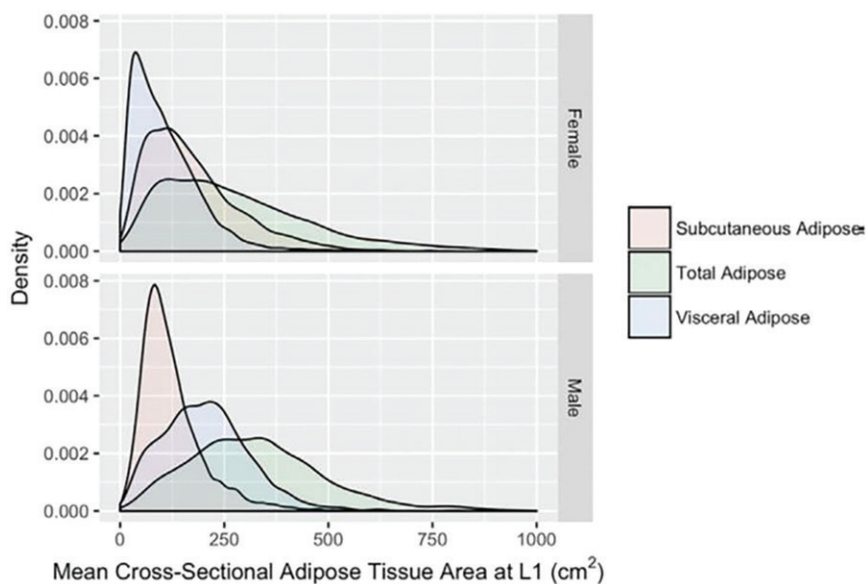


Figure 14. Density plots comparing the measurement of subcutaneous, visceral, and total adipose tissue according to sex. These density plots are derived from a large asymptomatic adult population and reflect automated CT-based measures at the L1 level. Note the relative distribution of subcutaneous and visceral fat between women and men, with men having more visceral fat than women, on average. The data on the y axis are the relative frequency of adipose tissue in the population studied. (Reprinted, with permission, from reference 22.)

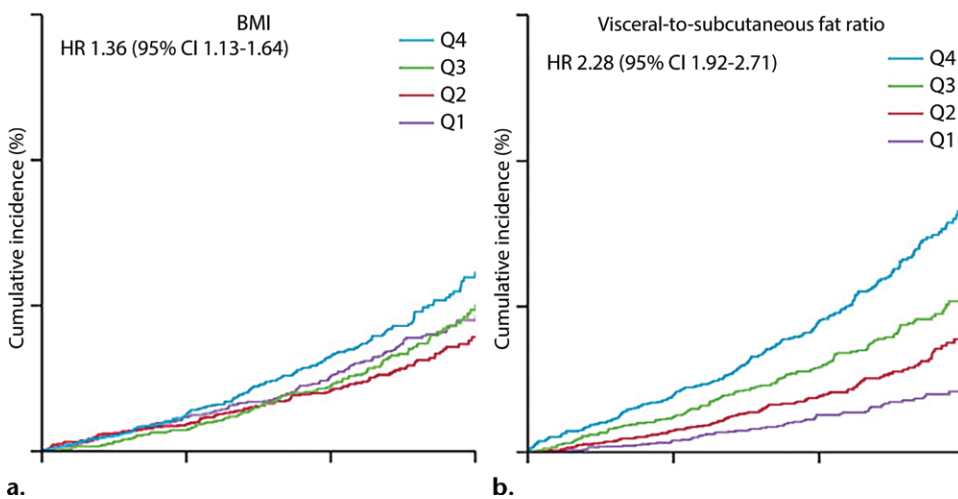
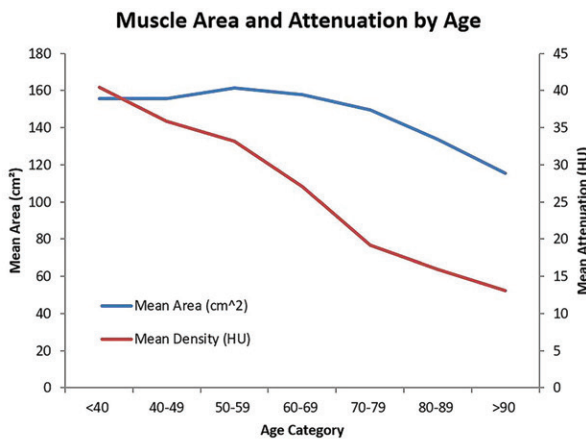
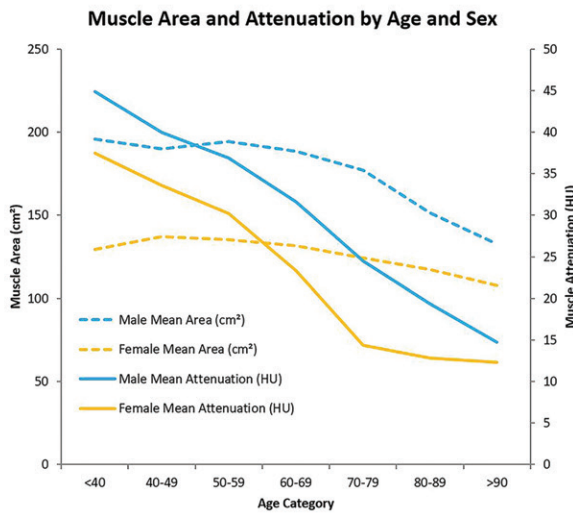


Figure 15. Kaplan-Meier time-to-death plots by quartile for automated CT-based body mass index (BMI) (a) and visceral to subcutaneous fat ratio (b) in a cohort of asymptomatic adults. Note how the separation among all four quartiles for visceral to subcutaneous fat ratio is substantially better than that for BMI, in which there is little difference among quartiles. This difference is also reflected in the larger hazard ratio (HR) between the highest-risk quartile (Q4) and the other three quartiles for the visceral to subcutaneous fat ratio compared with those for body mass index (2.3 vs 1.4). (Adapted and reprinted under a CC BY license from reference 23.)

muscle bulk for both men and women (Fig 16) and therefore may be a more sensitive indicator of sarcopenia (19). In our healthy outpatient adult screening cohort, mean muscle attenuation at noncontrast CT was 34 HU in men and 27 HU in women. We have also found that CT-based muscle attenuation translates into a more predictive biomarker than muscle bulk for future adverse events such as osteoporotic fractures, major cardiovascular events, and death (23,24). For example, we have shown that automated muscle attenuation alone outperforms the clinical reference standard of the FRAX tool for prediction of future hip fractures (Fig 17) (24), which are catastrophic complications of osteo-

porosis. In terms of overall survival, the highest-risk quartile based on muscle attenuation (<22 HU) was associated with a hazard ratio of 3.6 relative to the other three quartiles (23). As with other attenuation-based automated tools, a linear correction can be applied to contrast-enhanced CT to convert the value to a noncontrast equivalent (25).

The predictive value of muscle assessment appears to be complementary with other CT-based automated measurements of body composition. In particular, sarcopenic obesity has garnered substantial attention as an accelerated combined risk factor (64). The complementary predictive value of sarcopenic obesity is likely

**a.****b.****c.**

further enhanced when visceral fat is specifically taken into account. This is readily accomplished with the automated CT approach (65).

Quantification of Liver Fat

Nonalcoholic fatty liver disease is a widely prevalent condition and a major public health concern. Although the liver-specific risks for progression from fatty liver disease to nonalcoholic steatohepatitis and cirrhosis are legitimate concerns, the associated cardiovascular risks greatly outweigh them in terms of population health implications (Figs 10, 11) (66). Hepatic steatosis, or fatty liver disease, when it is not related to alcohol use or another identifiable cause (ie, nonalcoholic fatty liver disease), is now thought to be a critical component of or even a precursor to metabolic syndrome, although it is similar to visceral fat in that it is not part of the diagnostic criteria (59,60,67). We have found that body mass index is a very poor predictor of underlying liver fat content in individual patients (20). It is also important to recognize that liver attenuation at noncontrast CT has a linear relationship to the MRI-based proton density fat fraction (70–72), which allows individualized quantification of liver fat content at CT. Put in clinical context for routine practice, the noncontrast CT thresholds for mild steatosis (proton density fat fraction $\geq 5\%$) and moderate steatosis (proton density fat fraction $\geq 15\%$)

correspond to 57 HU and 40 HU, respectively (27). Previously, we studied hepatic steatosis at noncontrast CT by manually placing a single ROI in a representative area of the right hepatic lobe in each patient (9,10,73,74). Remarkably, a fully automated assessment of volumetric liver attenuation with the use of a deep-learning algorithm that consists of a modified three-dimensional U-Net is in close agreement with results of this manual ROI approach, with a mean difference of less than 3 HU (Fig 18) (20). This automated approach allows objective assessment of changes in liver fat content over time (Fig 19). Hepatic steatosis appears to represent an important complementary risk factor for prediction of future cardiovascular events (Figs 10, 11), presumably through the metabolic syndrome pathway (23). Unlike the other automated body composition tools to assess muscle, bone, calcium, and abdominal fat, simple conversion from contrast-enhanced CT to a noncontrast equivalent is not possible for liver fat content (27). Instead, only categorical assessment of contrast-enhanced CT (eg, moderate steatosis) is feasible.

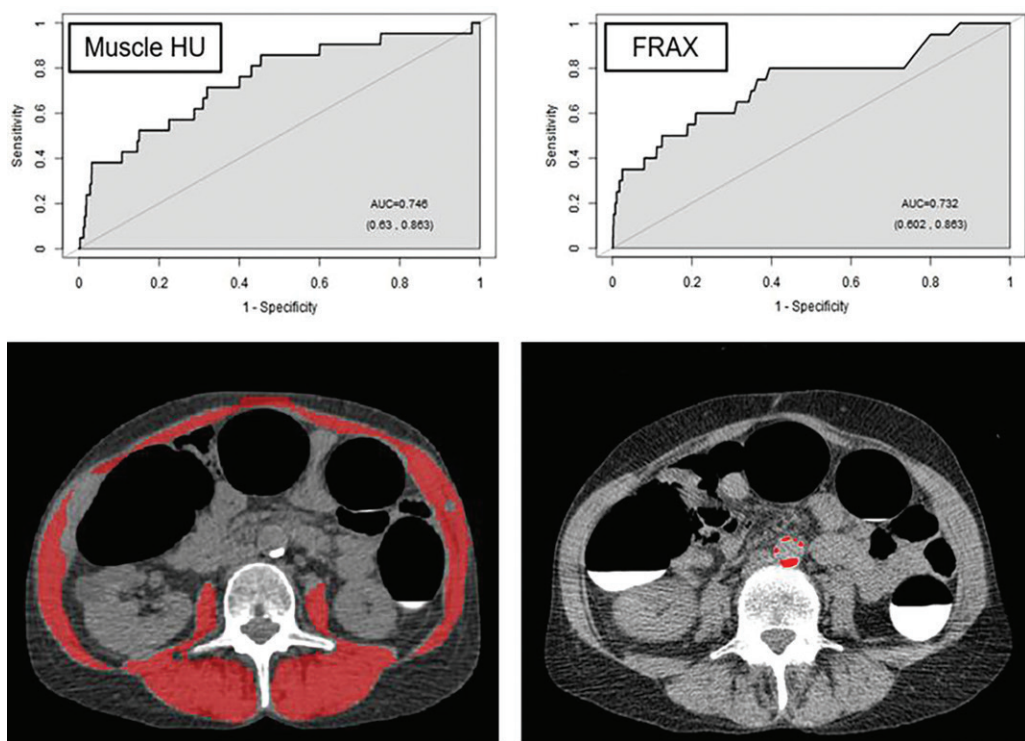


Figure 17. Sarcopenia for prediction of future hip fractures. ROC curves (top) for prediction of hip fractures over a 2-year period show that automated CT-based measurement of muscle attenuation in Hounsfield units (HU) alone (top left, AUC = 0.75) surpasses the multivariate FRAX score (top right, AUC = 0.73). When bone and muscle attenuation are combined (not shown), the performance is further improved (AUC = 0.76). Axial CT image (lower left) shows automated L3-level muscle segmentation in a 54-year-old asymptomatic woman. Mean muscle attenuation was -1.2 HU (98th percentile). Axial CT image (lower right) shows aortic calcium (red shading) with an automated Agatston score of 4283 (96th percentile). The patient had a myocardial infarction 3 months later, had a left hip fracture 1 year after that, and died 3 years later at age 58. (ROC curves reprinted, with permission, from reference 24.)

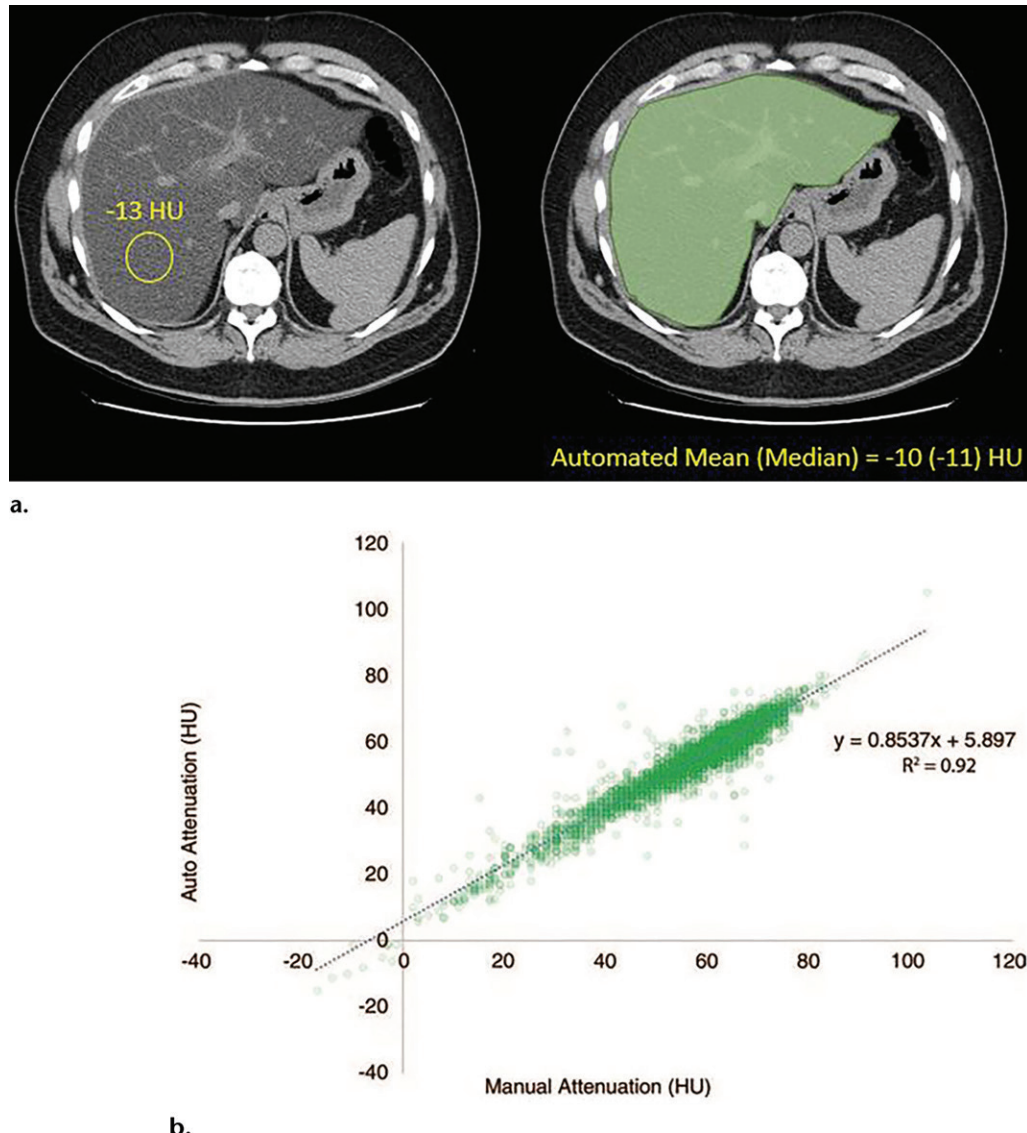
Quantifying liver fat at contrast-enhanced CT is more problematic. At portal venous phase imaging, comparison of the liver with the spleen allows gross categorization of steatosis (75), but not precise quantification. Deriving virtual non-contrast liver images from dual-energy CT would allow such quantification, assuming that attenuation values match closely with true noncontrast images.

Other Potential CT-based Biomarkers
A variety of additional CT-based measures could also serve as useful biomarkers, whether they are fully automated or not. Examples include CT-based radiomics and texture analysis, organ-based volumetry, and computer-aided strategies for detection and diagnosis (76–79). Some of these automated solutions such as computer-aided detection of colorectal polyps have been around for decades but can now be aimed at newer targets.

For nonalcoholic fatty liver disease and the related progression of liver disease, the relevant prognostic feature is neither steatosis nor nonalcoholic steatohepatitis, but rather the presence

of hepatic fibrosis (80,81). We have investigated several CT-based biomarkers for prediction of the degree of hepatic fibrosis, not only for nonalcoholic fatty liver disease, but also for hepatitis C and other causes of chronic liver disease (77,82–86). Specific measures have included liver surface nodularity (Fig 20), hepatosplenic volumetry, and texture analysis. Work is being done to automate fully some of these measures, which would help to facilitate opportunistic detection of unsuspected hepatic fibrosis. To date, we have developed a robust tool for automatically deriving liver and spleen volumes at CT. Although we have found that automated assessment of hepatic and splenic volume matches closely with semiautomated results, effective volumetric analysis of the liver for fibrosis requires Couinaud segmentation to derive the liver segmental volume ratio, which currently requires at least some manual interaction (77,86). Nonetheless, routine use of robust tools for automated derivation of total liver and spleen volume might one day supplant the current suboptimal approach that employs linear measurement for improved assessment of hepatomegaly and splenomegaly (Fig 21).

Figure 18. Automated versus manual liver fat quantification at noncontrast CT. (a) CT images at the same level show manual (left) and automated (right) methods for measuring liver attenuation (yellow circle, left; green shading, right) in an asymptomatic 60-year-old man with severe steatosis. (b) Scatterplot shows that the results of the manual ROI technique agree well with those of the automated volumetric approach. (Adapted and reprinted, with permission, from reference 20.)



Future Directions

The ultimate goal for these automated CT biomarkers is to leverage them for actual clinical implementation, which would allow prospective risk profiling in practice. Ideally, a dashboard readout with an automated structured report would be available at the time of initial interpretation by the radiologist. Given the rapid pace of artificial intelligence-based innovations in medical imaging, this could become a reality in the not-too-distant future. However, many challenges and hurdles remain. Additional validation in larger and more diverse cohorts is still required, which could be accelerated with a federated model. Regulatory approval, competing systems, workflow logistics, reimbursement models, potential

medical-legal issues, and even ethical considerations about opportunistic reporting must all be considered. In particular, the value proposition must be demonstrated convincingly, not only for the individual patient or imaging department but also for the entire system. Robust cost-effectiveness analyses that compare opportunistic screening with the clinical status quo (eg, DXA for osteoporosis screening) are needed. Of course, the former is essentially free information that was incidental to the indication for CT imaging.

The use of imaging data that are otherwise discarded for the benefit of patients is an easy position to defend. However, if it can be shown that combining multiple CT-based parameters provides a clear net clinical (and economic)

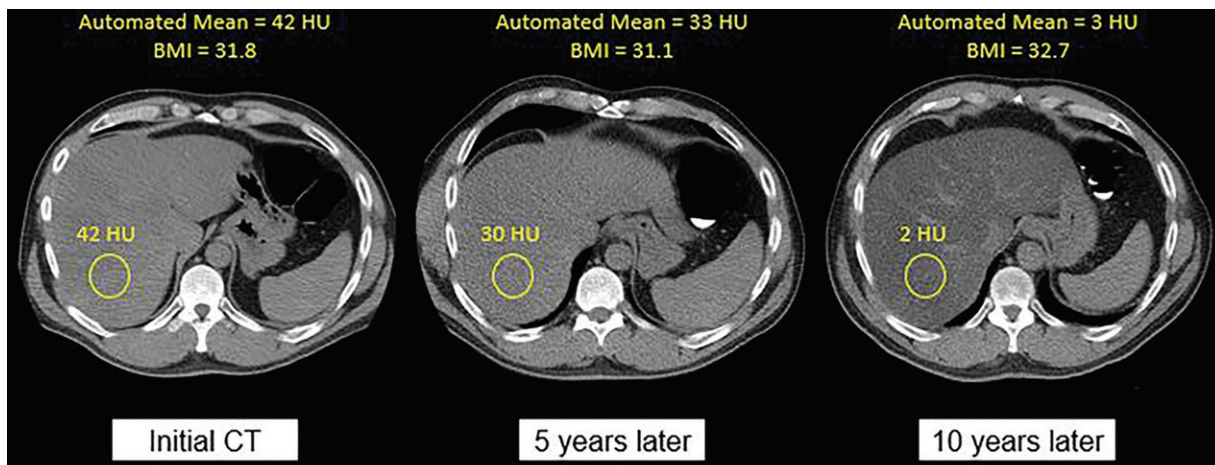
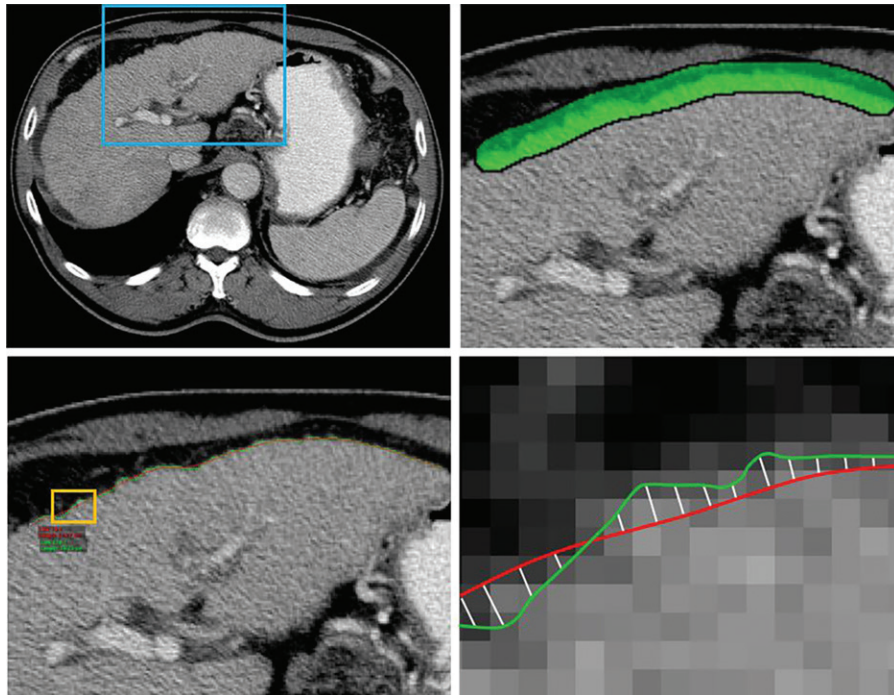


Figure 19. Changes in liver fat content over time. Axial noncontrast CT images acquired over a decade in an asymptomatic man who was 51 years of age at the time of initial imaging show substantial variation in liver attenuation in the ROI (yellow circle) corresponding to a liver fat fraction change of greater than 20%. Note the excellent agreement between the automated and manual measures of liver attenuation. Also note how little body mass index (BMI) has changed over time. (Reprinted, with permission, from reference 20.)

Figure 20. Semiautomated measurement of the liver surface nodularity score for detection of hepatic fibrosis and cirrhosis. Axial contrast-enhanced CT image (top left) of the liver in a patient with a hepatitis C virus infection who had not previously been evaluated with biopsy or noninvasive methods for liver fibrosis shows a cirrhotic liver with a nodular surface and trace ascites. The blue box shows the area that is magnified (magnification, $\times 2.5$) and appears in the upper right image, which shows how the liver is manually painted with the green brush stroke. Axial contrast-enhanced CT image (bottom left) shows automatic detection of the liver. The yellow box indicates the area that is magnified in the corresponding bottom right image. (Magnification, $\times 30$.) The green line represents the automatically detected liver surface, and the red line is a smoothed polynomial line (spline) fit to represent a smooth liver surface. The distances between the detected edge and spline are measured on a pixel-by-pixel basis, with approximately 100 measurements per section (bottom right) and 1000 measurements for the recommended 10 sections (not shown). The liver surface nodularity score in this case was 4.8, which is considered severe cirrhosis. (Case courtesy of Andrew D. Smith, MD.)



benefit, perhaps we can revisit the concept of intended or organized CT-based population screening. Of course, any such attempt must include consideration of the lessons learned from the previous whole-body CT screening fiasco, which lacked an evidence-based approach. The value of such a CT-based cardiometabolic screening strategy could also be further enhanced with simultaneous screening for colorectal cancer or possibly even lung cancer.

Conclusion

By leveraging the rich body composition data contained in all abdominal CT examinations with the power of artificial intelligence–based techniques, these automated measures offer the potential for presymptomatic detection of conditions that manifest with the greatest risk for future adverse events, such as osteoporotic fractures, major cardiovascular events, and death. The use of these automated biomarkers can match or exceed the

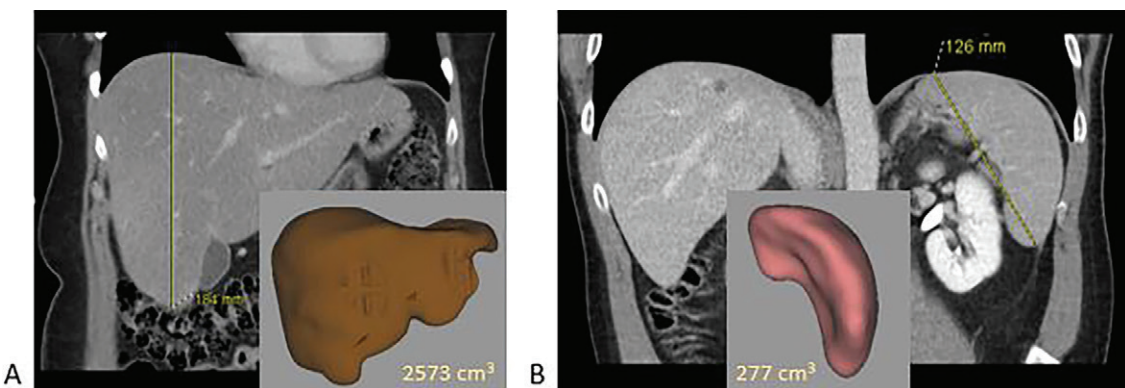


Figure 21. Automated hepatosplenic volumetry for improved assessment of hepatomegaly and splenomegaly. *A*, Coronal CT image in a 59-year-old woman shows a bulbous-appearing liver, but the maximal craniocaudal length was less than 20 cm. However, the automated liver volume was 2573 cm^3 , which is well above the upper limit of normal, derived as two standard deviations higher than the mean, as we describe in a currently unpublished study of an asymptomatic cohort. The segmented liver is shown on the inset image. *B*, Similarly, coronal CT image in a 45-year-old man shows a long-axis splenic measurement of greater than 12 cm, but the automated splenic volume of 277 cm^3 is well within the upper limit of the normal range and was established in a similar way. The segmented spleen is shown on the inset image. Note the normal crescentic shape of the spleen.

best available clinical prediction tools, which are somewhat onerous and often not obtained in clinical practice. When they are applied opportunistically during abdominal CT for other indications, these automated measures add value, especially for unscreened individuals. The potential value of this approach is further amplified by the large numbers of CT examinations that are performed for a wide variety of clinical indications.

Disclosures of Conflicts of Interest.—**P.J.P.** Activities related to the present article: consultancy for Zebra Medical. Activities not related to the present article: consultancy for Bracco; stock/stock options from Celleclectar, Elucent, and Shine. Other activities: disclosed no relevant relationships. **M.G.L.** Activities related to the present article: disclosed no relevant relationships. Activities not related to the present article: grants/grants pending from Ethicon and Philips. Other activities: disclosed no relevant relationships. **R.M.S.** Activities related to the present article: disclosed no relevant relationships. Activities not related to the present article: royalties from iCAD, Imbio, Ping An, Philips, ScanMed, Translation Holdings, and Zebra Medical; research support from Ping An and general processing unit card donation from Nvidia. Other activities: disclosed no relevant relationships.

References

- IMV Medical Information Division. IMV 2018 CT Market Outlook Report. Des Plaines, Ill: IMV Medical Information Division, 2018.
- Smith-Bindman R, Kwan ML, Marlow EC, et al. Trends in Use of Medical Imaging in US Health Care Systems and in Ontario, Canada, 2000–2016. *JAMA* 2019;322(9):843–856.
- Zalis ME, Barish MA, Choi JR, et al. CT colonography reporting and data system: a consensus proposal. *Radiology* 2005;236(1):3–9.
- Berland LL, Silverman SG, Gore RM, et al. Managing incidental findings on abdominal CT: white paper of the ACR incidental findings committee. *J Am Coll Radiol* 2010;7(10):754–773.
- Pooley BD, Kim DH, Pickhardt PJ. Extracolonic Findings at Screening CT Colonography: Prevalence, Benefits, Challenges, and Opportunities. *AJR Am J Roentgenol* 2017;209(1):94–102.
- Ziemlewicz TJ, Binkley N, Pickhardt PJ. Opportunistic Osteoporosis Screening: Addition of Quantitative CT Bone Mineral Density Evaluation to CT Colonography. *J Am Coll Radiol* 2015;12(10):1036–1041.
- Pickhardt PJ, Lee LJ, del Rio AM, et al. Simultaneous screening for osteoporosis at CT colonography: bone mineral density assessment using MDCT attenuation techniques compared with the DXA reference standard. *J Bone Miner Res* 2011;26(9):2194–2203.
- Pickhardt PJ, Pooler BD, Lauder T, del Rio AM, Bruce RJ, Binkley N. Opportunistic screening for osteoporosis using abdominal computed tomography scans obtained for other indications. *Ann Intern Med* 2013;158(8):588–595.
- Pickhardt PJ, Hahn L, Muñoz del Rio A, Park SH, Reeder SB, Said A. Natural history of hepatic steatosis: observed outcomes for subsequent liver and cardiovascular complications. *AJR Am J Roentgenol* 2014;202(4):752–758.
- Boyce CJ, Pickhardt PJ, Kim DH, et al. Hepatic steatosis (fatty liver disease) in asymptomatic adults identified by unenhanced low-dose CT. *AJR Am J Roentgenol* 2010;194(3):623–628.
- Pickhardt PJ, Jee Y, O'Connor SD, del Rio AM. Visceral adiposity and hepatic steatosis at abdominal CT: association with the metabolic syndrome. *AJR Am J Roentgenol* 2012;198(5):1100–1107.
- O'Connor SD, Graffy PM, Zea R, Pickhardt PJ. Does Non-enhanced CT-based Quantification of Abdominal Aortic Calcification Outperform the Framingham Risk Score in Predicting Cardiovascular Events in Asymptomatic Adults? *Radiology* 2019;290(1):108–115.
- Burns JE, Yao J, Chalhoub D, Chen JJ, Summers RM. A Machine Learning Algorithm to Estimate Sarcopenia on Abdominal CT. *Acad Radiol* 2020;27(3):311–320.
- Liu JM, Yao JH, Bagheri M, Sandfort V, Summers RM. A Semi-Supervised CNN Learning Method with Pseudo-class Labels for Atherosclerotic Vascular Calcification Detection. In: 2019 IEEE 16th International Symposium on Biomedical Imaging (ISBI 2019), Venice, Italy, April 8–11, 2019. Piscataway, NJ: IEEE, 2019; 780–783.
- Sandfort V, Yan K, Pickhardt PJ, Summers RM. Data augmentation using generative adversarial networks (CycleGAN) to improve generalizability in CT segmentation tasks. *Sci Rep* 2019;9(1):16884.
- Summers RM, Baecher N, Yao J, et al. Feasibility of simultaneous computed tomographic colonography and fully automated bone mineral densitometry in a single examination. *J Comput Assist Tomogr* 2011;35(2): 212–216.
- Weston AD, Korfiatis P, Kline TL, et al. Automated Abdominal Segmentation of CT Scans for Body Composition Analysis Using Deep Learning. *Radiology* 2019;290(3):669–679.

18. Graffy PM, Liu J, O'Connor S, Summers RM, Pickhardt PJ. Automated segmentation and quantification of aortic calcification at abdominal CT: application of a deep learning-based algorithm to a longitudinal screening cohort. *Abdom Radiol (NY)* 2019;44(8):2921–2928.
19. Graffy PM, Liu J, Pickhardt PJ, Burns JE, Yao J, Summers RM. Deep learning-based muscle segmentation and quantification at abdominal CT: application to a longitudinal adult screening cohort for sarcopenia assessment. *Br J Radiol* 2019;92(1100):20190327.
20. Graffy PM, Sandfort V, Summers RM, Pickhardt PJ. Automated Liver Fat Quantification at Nonenhanced Abdominal CT for Population-based Steatosis Assessment. *Radiology* 2019;293(2):334–342.
21. Pickhardt PJ, Lee SJ, Liu J, et al. Population-based opportunistic osteoporosis screening: Validation of a fully automated CT tool for assessing longitudinal BMD changes. *Br J Radiol* 2019;92(1094):20180726.
22. Lee SJ, Liu J, Yao J, Kanarek A, Summers RM, Pickhardt PJ. Fully automated segmentation and quantification of visceral and subcutaneous fat at abdominal CT: application to a longitudinal adult screening cohort. *Br J Radiol* 2018;91(1089):20170968.
23. Pickhardt PJ, Graffy PM, Zea R, et al. Automated CT biomarkers for opportunistic prediction of future cardiovascular events and mortality in an asymptomatic screening population: a retrospective cohort study. *Lancet Digit Health* 2020;2(4):e192–e200.
24. Pickhardt PJ, Graffy PM, Zea R, et al. Automated Abdominal CT Imaging Biomarkers for Opportunistic Prediction of Future Major Osteoporotic Fractures in Asymptomatic Adults. *Radiology* 2020;297(1):64–72.
25. Perez AA, Pickhardt PJ, Elton DC, Sandfort V, Summers RM. Fully automated CT imaging biomarkers of bone, muscle, and fat: correcting for the effect of intravenous contrast. *Abdom Radiol (NY)* 2020. 10.1007/s00261-020-02755-5. Published online September 18, 2020.
26. Summers RM, Elton DC, Lee S, et al. Atherosclerotic Plaque Burden on Abdominal CT: Automated Assessment With Deep Learning on Noncontrast and Contrast-enhanced Scans. *Acad Radiol* 2020. 10.1016/j.acra.2020.08.022. Published online September 18, 2020.
27. Pickhardt PJ, Blake GM, Graffy PM, et al. Liver Steatosis Categorization on Contrast-Enhanced CT Using a Fully-Automated Deep Learning Volumetric Segmentation Tool: Evaluation in 1,204 Healthy Adults Using Unenhanced CT as Reference Standard. *AJR Am J Roentgenol* 2020. 10.2214/AJR.20.24415. Published online September 16, 2020.
28. Burge R, Dawson-Hughes B, Solomon DH, Wong JB, King A, Tosteson A. Incidence and economic burden of osteoporosis-related fractures in the United States, 2005–2025. *J Bone Miner Res* 2007;22(3):465–475.
29. Khosla S, Hofbauer LC. Osteoporosis treatment: recent developments and ongoing challenges. *Lancet Diabetes Endocrinol* 2017;5(11):898–907.
30. Brauer CA, Coca-Perraillon M, Cutler DM, Rosen AB. Incidence and mortality of hip fractures in the United States. *JAMA* 2009;302(14):1573–1579.
31. Curtis JR, Carbone L, Cheng H, et al. Longitudinal trends in use of bone mass measurement among older Americans, 1999–2005. *J Bone Miner Res* 2008;23(7):1061–1067.
32. Ebeling PR. Clinical practice. Osteoporosis in men. *N Engl J Med* 2008;358(14):1474–1482.
33. Lee SJ, Pickhardt PJ. Opportunistic Screening for Osteoporosis Using Body CT Scans Obtained for Other Indications: the UW Experience. *Clin Rev Bone Miner Metab* 2017;15(3):128–137.
34. Siris ES, Chen YT, Abbott TA, et al. Bone mineral density thresholds for pharmacological intervention to prevent fractures. *Arch Intern Med* 2004;164(10):1108–1112.
35. Ziemlewicz TJ, Maciejewski A, Binkley N, Brett AD, Brown JK, Pickhardt PJ. Opportunistic Quantitative CT Bone Mineral Density Measurement at the Proximal Femur Using Routine Contrast-Enhanced Scans: Direct Comparison With DXA in 355 Adults. *J Bone Miner Res* 2016;31(10):1835–1840.
36. Pickhardt PJ, Bodeen G, Brett A, Brown JK, Binkley N. Comparison of femoral neck BMD evaluation obtained using Lunar DXA and QCT with asynchronous calibration from CT colonography. *J Clin Densitom* 2015;18(1):5–12.
37. Jang S, Graffy PM, Ziemlewicz TJ, Lee SJ, Summers RM, Pickhardt PJ. Opportunistic Osteoporosis Screening at Routine Abdominal and Thoracic CT: Normative L1 Trabecular Attenuation Values in More than 20 000 Adults. *Radiology* 2019;291(2):360–367.
38. Graffy PM, Lee SJ, Ziemlewicz TJ, Pickhardt PJ. Prevalence of Vertebral Compression Fractures on Routine CT Scans According to L1 Trabecular Attenuation: Determining Relevant Thresholds for Opportunistic Osteoporosis Screening. *AJR Am J Roentgenol* 2017;209(3):491–496.
39. Lee SJ, Anderson PA, Pickhardt PJ. Predicting Future Hip Fractures on Routine Abdominal CT Using Opportunistic Osteoporosis Screening Measures: A Matched Case-Control Study. *AJR Am J Roentgenol* 2017;209(2):395–402.
40. Boutin RD, Lenchik L. Value-Added Opportunistic CT: Insights Into Osteoporosis and Sarcopenia. *AJR Am J Roentgenol* 2020;215(3):582–594.
41. Lee SJ, Binkley N, Lubner MG, Bruce RJ, Ziemlewicz TJ, Pickhardt PJ. Opportunistic screening for osteoporosis using the sagittal reconstruction from routine abdominal CT for combined assessment of vertebral fractures and density. *Osteoporos Int* 2016;27(3):1131–1136.
42. Carberry GA, Pooler BD, Binkley N, Lauder TB, Bruce RJ, Pickhardt PJ. Unreported vertebral body compression fractures at abdominal multidetector CT. *Radiology* 2013;268(1):120–126.
43. Lee SJ, Graffy PM, Zea RD, Ziemlewicz TJ, Pickhardt PJ. Future Osteoporotic Fracture Risk Related to Lumbar Vertebral Trabecular Attenuation Measured at Routine Body CT. *J Bone Miner Res* 2018;33(5):860–867.
44. Pickhardt PJ, Lauder T, Pooler BD, et al. Effect of IV contrast on lumbar trabecular attenuation at routine abdominal CT: correlation with DXA and implications for opportunistic osteoporosis screening. *Osteoporos Int* 2016;27(1):147–152.
45. Dagan N, Elnekave E, Barda N, et al. Automated opportunistic osteoporotic fracture risk assessment using computed tomography scans to aid in FRAX underutilization. *Nat Med* 2020;26(1):77–82.
46. Burns JE, Yao J, Summers RM. Vertebral Body Compression Fractures and Bone Density: Automated Detection and Classification on CT Images. *Radiology* 2017;284(3):788–797.
47. Sidney S, Quesenberry CP Jr, Jaffe MG, et al. Recent Trends in Cardiovascular Mortality in the United States and Public Health Goals. *JAMA Cardiol* 2016;1(5):594–599.
48. Benjamin EJ, Blaha MJ, Chiuve SE, et al. Heart Disease and Stroke Statistics–2017 Update: A Report From the American Heart Association. *Circulation* 2017;135(10):e146–e603 [Published corrections appear in *Circulation* 2017;135(10):e646 and *Circulation* 2017;136(10):e196].
49. National Center for Health Statistics. Health, United States, 2016: With Chartbook on Long-term Trends in Health. <https://www.cdc.gov/nchs/data/hus/hus16.pdf#019>. Published 2017. Accessed March 26, 2020.
50. D'Agostino RB Sr, Vasan RS, Pencina MJ, et al. General cardiovascular risk profile for use in primary care: the Framingham Heart Study. *Circulation* 2008;117(6):743–753.
51. Yeboah J, Young R, McClelland RL, et al. Utility of Nontraditional Risk Markers in Atherosclerotic Cardiovascular Disease Risk Assessment. *J Am Coll Cardiol* 2016;67(2):139–147.
52. Nasir K, Clouse M. Role of nonenhanced multidetector CT coronary artery calcium testing in asymptomatic and symptomatic individuals. *Radiology* 2012;264(3):637–649.
53. Greenland P, LaBree L, Azen SP, Doherty TM, Detrano RC. Coronary artery calcium score combined with Framingham score for risk prediction in asymptomatic individuals. *JAMA* 2004;291(2):210–215.
54. Takayama Y, Yasuda Y, Suzuki S, et al. Relationship between abdominal aortic and coronary artery calcification as detected by computed tomography in chronic kidney disease patients. *Heart Vessels* 2016;31(7):1030–1037.
55. Wu MT, Yang P, Huang YL, et al. Coronary arterial calcification on low-dose ungent MDCT for lung cancer

- screening: concordance study with dedicated cardiac CT. *AJR Am J Roentgenol* 2008;190(4):923–928.
56. Stemmer A, Shadmi R, Bregman-Amitai O, et al. Using machine learning algorithms to review computed tomography scans and assess risk for cardiovascular disease: Retrospective analysis from the National Lung Screening Trial (NLST). *PLoS One* 2020;15(8):e0236021.
 57. Takx RAP, de Jong PA, Leiner T, et al. Automated coronary artery calcification scoring in non-gated chest CT: agreement and reliability. *PLoS One* 2014;9(3):e91239.
 58. Graffy PM, Pickhardt PJ. Quantification of hepatic and visceral fat by CT and MR imaging: relevance to the obesity epidemic, metabolic syndrome and NAFLD. *Br J Radiol* 2016;89(1062):20151024.
 59. Neeland IJ, Ross R, Després JP, et al. Visceral and ectopic fat, atherosclerosis, and cardiometabolic disease: a position statement. *Lancet Diabetes Endocrinol* 2019;7(9):715–725.
 60. Pickhardt PJ, Graffy PM, Zea R, et al. Utilizing Fully Automated Abdominal CT-Based Biomarkers for Opportunistic Screening for Metabolic Syndrome in Adults Without Symptoms. *AJR Am J Roentgenol* 2021;Jan;216 (1):85–92.
 61. Ryckman EM, Summers RM, Liu J, Munoz del Rio A, Pickhardt PJ. Visceral fat quantification in asymptomatic adults using abdominal CT: is it predictive of future cardiac events? *Abdom Imaging* 2015;40(1):222–226.
 62. Shah RV, Allison MA, Lima JA, et al. Abdominal fat radiodensity, quantity and cardiometabolic risk: The Multi-Ethnic Study of Atherosclerosis. *Nutr Metab Cardiovasc Dis* 2016;26(2):114–122.
 63. Pamoukdjian F, Bouillet T, Lévy V, Soussan M, Zelek L, Paillaud E. Prevalence and predictive value of pre-therapeutic sarcopenia in cancer patients: A systematic review. *Clin Nutr* 2018;37(4):1101–1113.
 64. Stenholm S, Harris TB, Rantanen T, Visser M, Kritchevsky SB, Ferrucci L. Sarcopenic obesity: definition, cause and consequences. *Curr Opin Clin Nutr Metab Care* 2008;11(6):693–700.
 65. Alalwan TA. Phenotypes of Sarcopenic Obesity: Exploring the Effects on Peri-Muscular Fat, the Obesity Paradox, Hormone-Related Responses and the Clinical Implications. *Geriatrics (Basel)* 2020;5(1):8.
 66. Anstee QM, Targher G, Day CP. Progression of NAFLD to diabetes mellitus, cardiovascular disease or cirrhosis. *Nat Rev Gastroenterol Hepatol* 2013;10(6):330–344.
 67. Lonardo A, Ballestri S, Marchesini G, Angulo P, Loria P. Nonalcoholic fatty liver disease: a precursor of the metabolic syndrome. *Dig Liver Dis* 2015;47(3):181–190.
 68. Targher G, Byrne CD, Lonardo A, Zoppini G, Barbui C. Non-alcoholic fatty liver disease and risk of incident cardiovascular disease: A meta-analysis. *J Hepatol* 2016;65(3):589–600.
 69. Wree A, Broderick L, Canbay A, Hoffman HM, Feldstein AE. From NAFLD to NASH to cirrhosis: new insights into disease mechanisms. *Nat Rev Gastroenterol Hepatol* 2013;10(11):627–636.
 70. Kramer H, Pickhardt PJ, Kliewer MA, et al. Accuracy of Liver Fat Quantification With Advanced CT, MRI, and Ultrasound Techniques: Prospective Comparison With MR Spectroscopy. *AJR Am J Roentgenol* 2017;208(1):92–100.
 71. Pickhardt PJ, Graffy PM, Reeder SB, Hernando D, Li K. Quantification of Liver Fat Content With Unenhanced MDCT: Phantom and Clinical Correlation With MRI Proton Density Fat Fraction. *AJR Am J Roentgenol* 2018;211(3):W151–W157.
 72. Guo Z, Blake GM, Li K, et al. Liver Fat Content Measurement with Quantitative CT Validated against MRI Proton Density Fat Fraction: A Prospective Study of 400 Healthy Volunteers. *Radiology* 2020;294(1):89–97.
 73. Pickhardt PJ, Park SH, Hahn L, Lee SG, Bae KT, Yu ES. Specificity of unenhanced CT for non-invasive diagnosis of hepatic steatosis: implications for the investigation of the natural history of incidental steatosis. *Eur Radiol* 2012;22(5):1075–1082.
 74. Hahn L, Reeder SB, Muñoz del Rio A, Pickhardt PJ. Longitudinal Changes in Liver Fat Content in Asymptomatic Adults: Hepatic Attenuation on Unenhanced CT as an Imaging Biomarker for Steatosis. *AJR Am J Roentgenol* 2015;205(6):1167–1172.
 75. Kim DY, Park SH, Lee SS, et al. Contrast-enhanced computed tomography for the diagnosis of fatty liver: prospective study with same-day biopsy used as the reference standard. *Eur Radiol* 2010;20(2):359–366.
 76. Lubner MG, Smith AD, Sandrasegaran K, Sahani DV, Pickhardt PJ. CT Texture Analysis: Definitions, Applications, Biologic Correlates, and Challenges. *RadioGraphics* 2017;37(5):1483–1503.
 77. Pickhardt PJ, Malecki K, Hunt OF, et al. Hepatosplenic volumetric assessment at MDCT for staging liver fibrosis. *Eur Radiol* 2017;27(7):3060–3068.
 78. Summers RM, Yao J, Pickhardt PJ, et al. Computed tomographic virtual colonoscopy computer-aided polyp detection in a screening population. *Gastroenterology* 2005;129(6):1832–1844.
 79. Summers RM. Progress in Fully Automated Abdominal CT Interpretation. *AJR Am J Roentgenol* 2016;207(1):67–79.
 80. Ekstedt M, Hagström H, Nasr P, et al. Fibrosis stage is the strongest predictor for disease-specific mortality in NAFLD after up to 33 years of follow-up. *Hepatology* 2015;61(5):1547–1554.
 81. Angulo P, Kleiner DE, Dam-Larsen S, et al. Liver Fibrosis, but No Other Histologic Features, Is Associated With Long-term Outcomes of Patients With Nonalcoholic Fatty Liver Disease. *Gastroenterology* 2015;149(2):389–97.e10.
 82. Lubner MG, Malecki K, Kloke J, Ganeshan B, Pickhardt PJ. Texture analysis of the liver at MDCT for assessing hepatic fibrosis. *Abdom Radiol (NY)* 2017;42(8):2069–2078.
 83. Lubner MG, Pickhardt PJ. Multidetector Computed Tomography for Retrospective, Noninvasive Staging of Liver Fibrosis. *Gastroenterol Clin North Am* 2018;47(3):569–584.
 84. Pickhardt PJ, Graffy PM, Said A, et al. Multiparametric CT for Noninvasive Staging of Hepatitis C Virus-Related Liver Fibrosis: Correlation With the Histopathologic Fibrosis Score. *AJR Am J Roentgenol* 2019;212(3):547–553.
 85. Pickhardt PJ, Malecki K, Kloke J, Lubner MG. Accuracy of Liver Surface Nodularity Quantification on MDCT as a Noninvasive Biomarker for Staging Hepatic Fibrosis. *AJR Am J Roentgenol* 2016;207(6):1194–1199.
 86. Furusato Hunt OM, Lubner MG, Ziemslewicz TJ, Muñoz Del Rio A, Pickhardt PJ. The Liver Segmental Volume Ratio for Noninvasive Detection of Cirrhosis: Comparison With Established Linear and Volumetric Measures. *J Comput Assist Tomogr* 2016;40(3):478–484.